Joule

Article

Guidelines for correlative imaging and analysis of reactive alkali metal battery materials

Graphical abstract

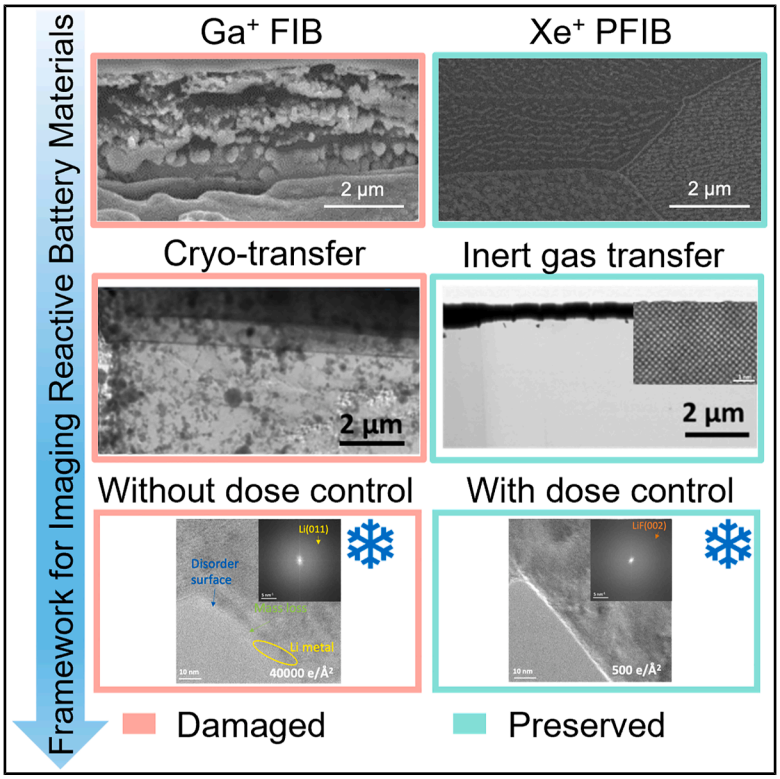

Highlights

- Framework for artifact-free imaging of reactive alkali metals and SEIs
- Room-temperature atomic-resolution imaging of lithium metal achieved
- Cryogenic, low-dose conditions required for beam-sensitive SEI phases
- Inert-gas sample transfer with PFIB enables damage-free preparation of alkali metal samples

Authors

Shuang Bai, Zhao Liu, Diyi Cheng, ..., Alexander Bright, Minghao Zhang, Ying Shirley Meng

Correspondence

miz016@uchicago.edu (M.Z.), shirleymeng@uchicago.edu (Y.S.M.)

In brief

Reactive alkali metals are central to next-generation batteries, yet their extreme sensitivity has long complicated reliable imaging. This study establishes a unified workflow—from storage to ion-beam milling to electron microscopy—that preserves the native structure and chemistry of lithium and sodium metals and their SEIs. By clarifying when cryogenic conditions are required and identifying dose limits for beam-sensitive phases, the work provides a foundation for reproducible, artifact-free characterization across the battery community.

Bai et al., 2026, Joule *10*, 102311
April 15, 2026
https://doi.org/10.1016/j.joule.2025.102311

CellPress

Please cite this article in press as: Bai et al., Guidelines for correlative imaging and analysis of reactive alkali metal battery materials, Joule (2025), https://doi.org/10.1016/j.joule.2025.102311

Joule

CellPress

Article

Guidelines for correlative imaging and analysis of reactive alkali metal battery materials

Shuang Bai,[1,2,3,6] Zhao Liu,[4,6] Diyi Cheng,[3] Bingyu Lu,[5] Nestor J. Zaluzec,[2] Ganesh Raghavendran,[3] Shen Wang,[5] Thomas S. Marchese,[1,2] Brandon van Leer,[4] Letian Li,[4] Lin Jiang,[4] Adam Stokes,[4] Joseph P. Cline,[4] Rachel Osmundsen,[4] Minda Chen,[4] Paul Barends,[4] Alexander Bright,[4] Minghao Zhang,[1,2,*] and Ying Shirley Meng[1,2,5,7,*]

[1]Energy Storage Research Alliance, Argonne National Laboratory, Lemont, IL 60439, USA
[2]Pritzker School of Molecular Engineering, University of Chicago, Chicago, IL 60637, USA
[3]Program of Materials Science and Engineering, University of California, San Diego, La Jolla, CA 92093, USA
[4]Thermo Fisher Scientific, Hillsboro, OR 97124, USA
[5]Aiiso Yufeng Li Family Department of Chemical and Nano Engineering, University of California, San Diego, La Jolla, CA 92093, USA
[6]These authors contributed equally
[7]Lead contact
*Correspondence: miz016@uchicago.edu (M.Z.), shirleymeng@uchicago.edu (Y.S.M.)
https://doi.org/10.1016/j.joule.2025.102311

CONTEXT & SCALE Understanding how reactive alkali metals behave during battery operation is central to advancing next-generation energy storage, yet their extreme sensitivity to air, moisture, and electron or ion probes has long limited reliable characterization. Lithium and sodium metals, along with their solid electrolyte interphases (SEIs), undergo rapid chemical and beam-induced transformations that can obscure their native structure. This study establishes a unified framework—from storage and focused ion beam (FIB) preparation to transfer and electron microscopy—that clarifies when cryogenic conditions are essential and when room-temperature imaging is feasible. A key conceptual finding is that metallic alkali phases and their SEIs possess fundamentally different beam tolerances: lithium metal can be imaged at atomic resolution at room temperature if air exposure is eliminated, whereas common SEI components such as Li_2CO_3 and LiF require low-dose cryogenic conditions to avoid artificial reduction or decomposition.

Equally important, this work reveals that widely used preparation tools can introduce substantial artifacts unless chemical reactivity is explicitly considered. Inert plasma FIB sources such as Xe^+ or Ar^+ mill alkali metals without structural distortion, while conventional Ga^+ FIB induces alloying and morphological damage. By quantifying dose limits, defining reliable transfer protocols, and identifying sources of artifacts, this framework enables reproducible, artifact-free imaging across length scales. It provides the broader energy community with a standardized foundation for probing reactive metal interfaces critical to high-performance alkali metal batteries.

SUMMARY

Reliable characterization of alkali metals and their solid electrolyte interphases (SEIs) is essential for advancing high-energy batteries but remains difficult due to their extreme reactivity and beam sensitivity. This work redefines the experimental limits for high-resolution imaging of lithium and sodium metals. Contrary to prevailing assumptions, we show that atomic-resolution transmission electron microscopy (TEM) of lithium metal is achievable at room temperature using inert-gas sample transfer, with electron dose rates above 10^3 e/Å^2·s causing no structural damage. SEI phases such as Li_2CO_3 and Na_2CO_3 remain highly beam-sensitive and require cryogenic TEM and strict dose control. We further demonstrate that plasma-focused ion beam (plasma-FIB) milling enables artifact-free lithium lamella preparation at ambient conditions, unlike conventional Ga^+ FIB. Systematic evaluation of environmental, electron, and ion-beam effects also reveals inconsistencies arising from non-standardized cryogenic workflows. This framework provides a reproducible, damage-minimized pathway for imaging reactive metals and interfaces in next-generation batteries.

Please cite this article in press as: Bai et al., Guidelines for correlative imaging and analysis of reactive alkali metal battery materials, Joule (2025), https://doi.org/10.1016/j.joule.2025.102311

INTRODUCTION

Reactive alkali metal batteries, including those based on lithium and sodium, have emerged as promising candidates for next-generation energy storage, offering the potential to significantly improve the performance of electric vehicles, drones, and portable electronics.[1] Lithium metal, with its high specific capacity (3,860 mAh/g) and low electrochemical potential (−3.04 V vs. standard hydrogen electrode [SHE]), represents an ideal anode material for achieving ultrahigh energy density.[2] Similarly, sodium metal offers cost-effective scalability and fast ion transport,[3] positioning it as a compelling alternative for grid-scale storage.[4] However, the practical deployment of reactive metal anodes is hindered by short cycle life and safety concerns, primarily due to dendritic growth and the formation of electrochemically inactive phases. Central to these challenges is the morphology and composition of the deposited metal and its solid electrolyte interphase (SEI), which governs ion transport and interfacial stability.[5] The SEI acts as a passivation layer, suppressing parasitic reactions while maintaining Li^+ or Na^+ conductivity, and its structural and chemical integrity is critical to the reversibility of metal plating and stripping.[6–8] These processes involve complex, multiscale phenomena including electron transfer, ion diffusion, interphase formation, and mechanical evolution.[9–11] As such, comprehensive, correlative characterization techniques that bridge micro- and nanoscale resolution[12,13] are essential to reveal the coupled chemo-mechanical dynamics at reactive metal interfaces and to inform rational design strategies for stable, high-performance alkali metal batteries.

The rapid progress in cryogenic electron microscopy (cryo-EM) empowers researchers with new tools and methods to probe many otherwise inaccessible length scales and time scales of components and phenomena in electrochemical energy science. By stabilizing alkali metal samples below −170°C in a high-vacuum environment (<10^{-4} Pa), contamination from moisture and oxygen can be minimized, and electron beam-induced damage to the samples is greatly mitigated. These advanced cryogenic imaging methods have been recently applied to study non-biological irradiation-sensitive materials such as the lithium metal anode and the SEI in batteries.[12,14–17] The structure of alkali metal anodes and their nanostructured SEI species has been resolved using cryogenic transmission electron microscopy (cryo-TEM).[8,14,15,18] Furthermore, cryogenic-focused ion-beam techniques (cryo-FIB) have been introduced to the battery field, enabling the examination of electrodeposited alkali metal at the scale of hundreds of microns.[8,17] Importantly, cryo-FIB allows for the precise thinning of alkali metal samples to below 100 nm while minimizing material damage, thereby making them suitable for detailed TEM analysis.

Due to the high reactivity of both alkali metals and the SEI with environmental factors and external probes, maintaining sample integrity during correlative characterization across multiple analytical tools and length scales poses a significant challenge. Specifically, when, where, and how to employ cryogenic imaging techniques in battery studies remains a topic of debate without proper characterization protocols. Recent reports have demonstrated atomic-resolution TEM imaging of Li metal without inducing irradiation damage,[19] even at room temperature, with a dose rate exceeding 1,000 e/Å^2·s, challenging the prior notion that cryo-EM is indispensable for Li metal imaging.[14] Additionally, unlike Ga^+, it has been observed that the emerging plasma FIB (PFIB) technique, utilizing Xe^+, does not introduce any discernible morphological changes, such as new gaps or voids, in Li metal or at the interface during milling at room temperature.[20] The complex nature of cryo-EM characterization also poses a significant challenge, as it allows for the generation of discrepancies at various stages of operation due to diverse sample handling protocols without standardization. These uncertainties are particularly prevalent during the sample transfer procedure.

This study presents a correlative imaging framework for the reliable characterization of reactive battery materials, using lithium and sodium metals, along with their respective SEIs, as model systems. We systematically examine their sensitivity to environmental exposure and beam-induced artifacts across various stages of specimen preparation and imaging. Correlative imaging in this work refers to the integration of imaging techniques across multiple length scales, allowing direct structural and chemical correlation of the same region. First, we investigate the stability of electrochemically deposited lithium stored under an inert argon atmosphere, quantifying active material loss over time and identifying the critical time window for sample storage. We then evaluate the impact of different FIB sources—including Ga^+, Xe^+, and Ar^+—on specimen integrity, revealing that noble gases such as Xe enable contamination-free cross-section preparation at room temperature. To address challenges associated with cryo-EM, we assess multiple transfer protocols and their influence on sample contamination and structural fidelity. Finally, we explore the interplay between electron dose and cryogenic conditions during high-resolution imaging, establishing threshold conditions for preserving alkali metal and SEI structures. Integrating these findings, we propose a robust, end-to-end protocol that ensures the preservation of native chemistry and morphology from storage to atomic-level imaging.

RESULTS & DISCUSSION

Storage and FIB preparation of alkali metal

A critical initial challenge in this study was determining the shelf life of alkali metal electrodes following battery cycling. While it is standard practice to store disassembled electrodes in an argon-filled glovebox (<0.1 ppm O_2/H_2O), residual impurities can still react with alkali metals over time, forming Li_2O/Na_2O, LiOH/NaOH, and Li_2CO_3/Na_2CO_3 that compromise surface chemistry. These effects are further intensified by cycling-induced morphological changes—such as increased roughness and surface area. To quantitatively assess lithium degradation during storage, we employed titration gas chromatography (TGC)[1] to measure the loss of active lithium in three representative samples: commercial lithium foil and electrochemically deposited lithium using either a Gen2 electrolyte (1.2 M $LiPF_6$ in EC:EMC) or a high-concentration bisalt electrolyte (4.7 M LiFSI + 2.3 M LiTFSI in 1,2-dimethoxyethane [DME]). Despite identical glovebox storage conditions, substantial differences in lithium retention were observed (Figure 1A). After 7 days, the Gen2 sample exhibited >40% loss in Li^0 content, compared with <10% in

Please cite this article in press as: Bai et al., Guidelines for correlative imaging and analysis of reactive alkali metal battery materials, Joule (2025), https://doi.org/10.1016/j.joule.2025.102311

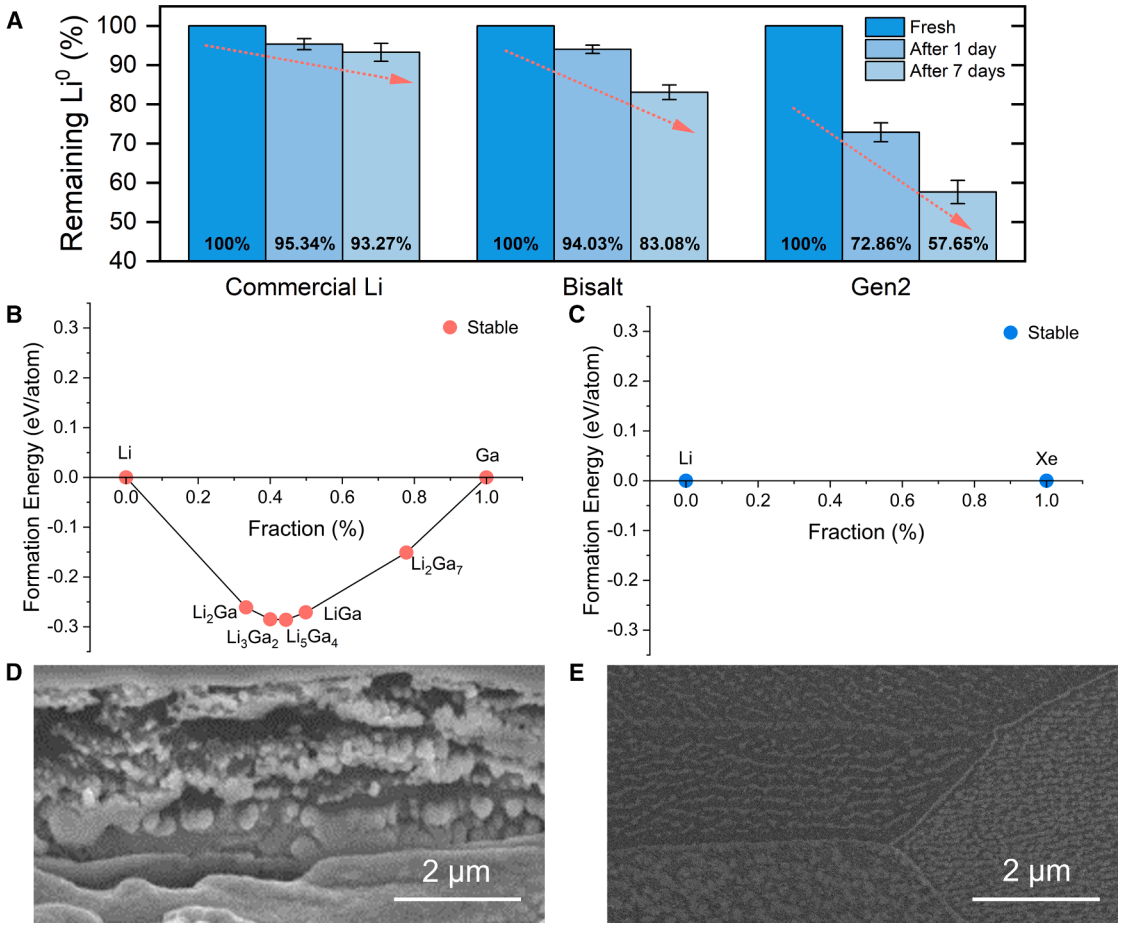

Figure 1. Storage test of different lithium metals in an Ar-filled glovebox and evaluation of the ion-beam-induced morphological and compositional change of lithium metal in Ga^+ FIB and Xe^+ PFIB

(A) Comparison of Li metal inventory loss, tested by TGC, among commercial lithium, electrochemically deposited lithium in bisalt electrolyte (0.25 mAh/cm^2 at 2 mA/cm^2), and electrochemically deposited lithium in Gen2 electrolyte (0.25 mAh/cm^2 at 2 mA/cm^2). Data are presented as the mean values with error bars representing the minimum and maximum values measured from a set of three samples at same conditions.

(B and C) Calculated alloy phases of (B) the Li-Ga system and (C) the Li-Xe system. The phase diagram is constructed based on the data from the Materials Project.

(D and E) Cross-section images of commercial lithium foil ion milled at room temperature using (D) Ga^+ FIB with a 3 nA milling current and (E) Xe^+ PFIB with a 1 μA milling current.

commercial lithium and ~20% in the bisalt sample. These variations arise from differences in microstructure and SEI composition[2,21]: compact commercial Li exhibits superior passivation, while dendritic Li with organic-rich SEI—especially in the Gen2 system—remains highly reactive. Improved SEI stability from the bisalt electrolyte affords better resistance to environmental degradation, highlighting the importance of deposition chemistry in post-cycling storage stability.

Figure S1 shows the morphological evolution of lithium samples during storage, correlating TGC-measured Li^0 loss with observable microstructural degradation. For commercial Li foil, no obvious morphological change occurs after 1 day, and only minor surface contamination is detected after 7 days. By contrast, electrochemically deposited Li metal in Gen2 electrolyte exhibits substantial surface voids and strong charging effects after 1 day of storage, consistent with insulating surface film formation and Li^0 depletion. These changes can lead to misinterpretation of surface porosity or SEI morphology as electrochemical features. To preserve native structure and chemistry, correlative EM should ideally be conducted within 1–2 days of preparation, and within a few hours for highly reactive or low Coulombic efficiency systems, thereby minimizing air/moisture interaction and residual contaminant reactions within the glovebox. For laboratories equipped with TGC, we recommend conducting glovebox-specific assessments to establish appropriate storage time limits tailored to their electrode chemistries. Notably, sodium metal exhibits even greater environmental sensitivity than lithium and may require immediate processing post-disassembly to preserve structural and chemical integrity.

High-quality imaging of alkali metals requires minimal environmental contamination and beam-induced damage. FIB is a preferred method due to its precision and compatibility with

Please cite this article in press as: Bai et al., Guidelines for correlative imaging and analysis of reactive alkali metal battery materials, Joule (2025), https://doi.org/10.1016/j.joule.2025.102311

high-vacuum conditions, which help limit exposure to ambient gases. However, conventional Ga^+ FIB milling at room temperature induces severe morphological degradation in lithium, even at low beam currents (e.g., 3 nA at 30 kV), as shown in Figure 1D. This finding aligns with our prior observations, highlighting the necessity of cryogenic conditions to mitigate adverse side effects.[17] Several mechanisms have been proposed to explain this protective effect: (1) at room temperature under high vacuum ($\sim 10^{-4}$ Pa), bulk lithium is susceptible to local beam heating, leading to melting and evaporation, and (2) Ga^+ ions exhibit deep implantation (>500 nm), enabling the formation of Ga-Li alloy phases that deform the structure. To isolate the role of chemical reactivity, we evaluated Xe^+ PFIB as a chemically inert alternative. Our thermodynamic analysis (Figures 1B and 1C) and experimental results reveal that Ga^+ readily forms Li-Ga alloys, causing deformation and structural loss, while Xe^+ remains non-reactive and preserves bulk morphology, even at significantly higher beam currents exceeding 1 μA. Notably, Xe^+ PFIB milling retained clear grain boundaries and crystalline features, enabling artifact-free SEM imaging (Figure 1E). Comparable results were also obtained using other noble gases such as Ar^+ PFIB (Figure S2), further supporting that chemical reactivity, rather than beam heating, is the dominant factor responsible for beam-induced damage.

In addition to evaluating the ion-beam-induced morphological effects, the compositional changes in lithium metal resulting from (P)FIB milling were also characterized. X-ray energy dispersive spectroscopy (EDS) integrated into the (P)FIB instruments, which were employed for these studies, was used to monitor changes in the nominal composition of the lithium specimen. The higher reactivity between Ga and Li leads to an implantation of Ga in the specimen, which is readily detectable using EDS (Figure S3), while similar experiments conducted in the Xe^+ PFIB demonstrate a nearly undetectable Xe signal, confirming the chemical inertness of noble gas plasma ions.

Regardless of the ion source, surface contamination from oxygen is unavoidable at room temperature, even when experiments are conducted under oxygen partial pressures below 10^{-5} Pa. A recorded video (Video S1) captures the sequence of contamination on a pristine lithium metal surface upon exposure within the PFIB chamber. This surface contamination can be moderated by performing PFIB milling under cryogenic conditions, as demonstrated in Figure S4. These findings highlight the necessity of optimizing specimen preparation conditions, including storage time, ion source, and temperature, to maintain the structural and chemical fidelity of reactive alkali metals. While room-temperature PFIB enables high-throughput, damage-free bulk sectioning, cryogenic conditions remain indispensable for interfacial investigations at the nanoscale.

Alkali metal transfer for TEM imaging

In this section, we propose to address the critical role of sample transfer in preserving the integrity of reactive alkali metals. This process involves two key stages: (1) transferring the alkali metal sample from the glovebox to the (P)FIB system for lamella preparation and subsequently returning it to the glovebox and (2) transferring the prepared lamella from the glovebox to the TEM. For the first stage, we propose the use of the inert gas sample transfer (IGST) system, which is specifically designed to maintain an inert transfer environment. This system enables sample movement between the glovebox and PFIB-SEM under overpressurized argon protection, thereby minimizing exposure to ambient air and moisture.

The second stage for preserving the lamella integrity from PFIB-SEM to TEM via glovebox is even more critical and challenging, as the lamella has a higher surface area to bulk ratio than the bulk alkali metals, thus being more reactive. So far, two commercially available holders[22] have been applied to enable cryo-TEM characterization: the cryo-transfer holder and the cooling holder. The cryo-transfer holder is designed to precool the holder before loading the cryogenically prepared sample grid onto it while emersed in liquid nitrogen.[23,24] This method is widely employed for biological samples, as it effectively maintains the sample integrity in a frozen cryogenic state and reduces sample reactivity. The principal advantage of such rapid flash-freezing is that it preserves the native room-temperature structure by minimizing atomic diffusion and interfacial reconstruction during cooling. This approach effectively "quenches" metastable or reactive configurations that would otherwise relax or degrade under slower cooling, making it particularly beneficial for capturing transient SEI morphologies or electrolyte decomposition products. However, during the process of loading the grid onto the holder and transferring the sample to TEM, some frozen water inevitably forms on the sample (Figure 2A). To mitigate this, strict humidity control around the TEM is essential, which can limit compatibility with available instrumentation. Additionally, vacuum system outgassing is a secondary source of water vapor, and employing cryo-fingers in the TEM is necessary to minimize condensation.

By contrast, the cooling holder cools the sample only after insertion into the TEM column. While it allows for handling under an inert atmosphere, typically using a glove bag, brief air exposure during insertion is unavoidable due to incomplete environmental isolation. Any short exposure of samples to air could lead to changes in sample surface morphology and chemistry due to contamination. An example of which is shown in Figure S5. Here, with only 15 s of exposure to air, the scanning transmission electron microscopy (STEM) dark field and high angular dark field images show significant structural changes of Li metal. The particulate and network-shaped contrast on the surface of the lamella is indicative of oxidation or carbonation (Figure 2B).

These findings suggest that ideal sample transfer for alkali metal TEM characterization must fully prevent air exposure and minimize ice formation. To meet these requirements, we employed an inert gas transfer holder. As shown in Figure 2C, the inert gas transfer holder features a retractable tip with an O-ring seal, enabling secure enclosure of the specimen within an argon-filled glovebox. This design effectively shields the sample from ambient air during transfer and eliminates ice formation by operating at room temperature in a low-moisture environment. Once inserted into the TEM vacuum system, the sealed compartment can be opened without compromising sample integrity. A recent study also compared cryo- and room-temperature transfer of Li dendrites using different holders.[25] In that work, the so-called 'vacuum-transfer holder' sealed the sample

Please cite this article in press as: Bai et al., Guidelines for correlative imaging and analysis of reactive alkali metal battery materials, Joule (2025), https://doi.org/10.1016/j.joule.2025.102311

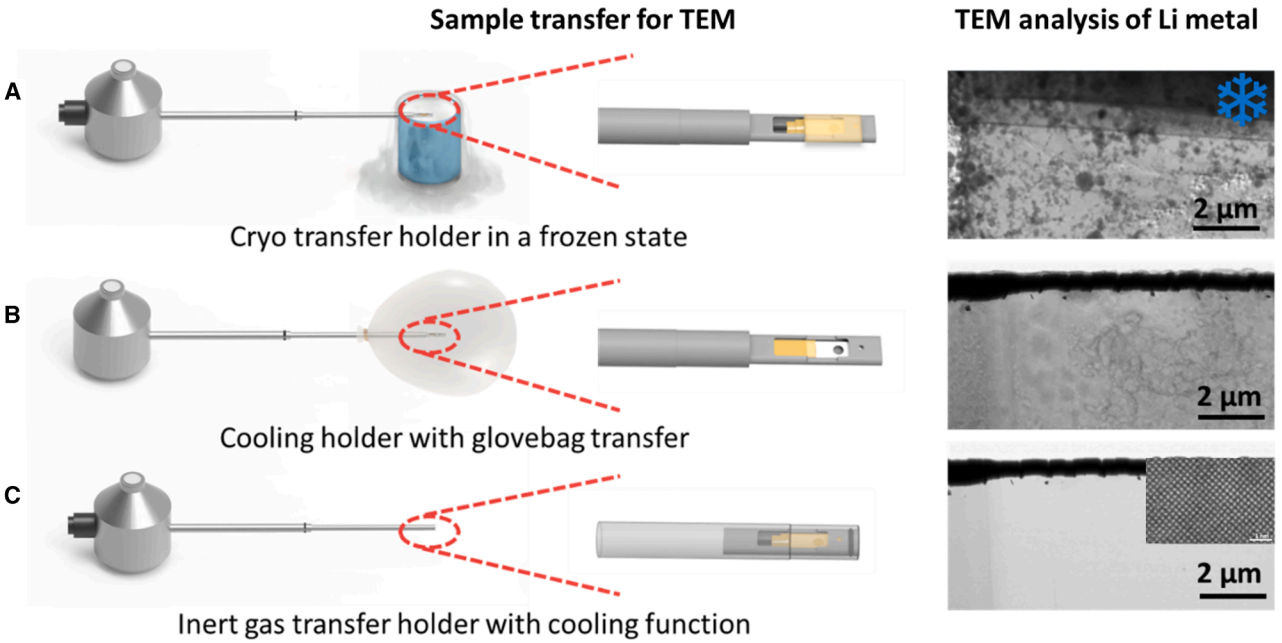

Figure 2. Correlative imaging workflow for TEM through different sample transfer methods to observe reactive lithium metal down to the atomic scale

(A) Cryo-transfer holder: sample pre-cooled and maintained under cryogenic conditions, minimizing reactivity but susceptible to ice formation from residual moisture.

(B) Cooling holder with glovebag transfer: sample handled under inert atmosphere and cooled post-insertion, allowing brief air exposure that can cause surface oxidation.

(C) Inert gas transfer holder with cooling function: sample sealed in an argon-filled, O-ring enclosed chamber for fully air-free transfer without ice formation, preserving native morphology and chemistry for high-resolution imaging.

under vacuum, susceptible to air leakage due to external overpressure. By contrast, our optimized inert gas transfer holder maintains a positive internal Ar pressure relative to the environment, providing improved protection against leakage. Minimal surface contamination was observed under inert gas transfer conditions, as demonstrated in Figure 2C. A direct comparison with samples exposed to air for just 15 s (Figures S5 and S6) reveals that inert gas transfer preserves both morphology and chemistry, allowing high-resolution TEM imaging of Li metal at room temperature. Notably, even under a high electron dose rate of 3.5×10^3 e/Å^2·s and a total dose of 1,750 e/Å^2, no discernible irradiation damage was detected, validating this protocol for artifact-free, correlative imaging. This observation aligns with a recent study that reported the visualization of alkali metal growth with millisecond temporal resolution at room temperature.[19] These findings indicate the electron beam reactivity of the electrochemically deposited Li metal in the previous studies[15,26,27] is mainly due to its SEI components instead of the metallic bulk structure.

While room-temperature imaging of lithium metal is achievable with careful sample transfer, sodium metal presents an even greater challenge due to its higher chemical reactivity. Even under ultrahigh vacuum conditions ($\sim10^{-6}$ Pa) in the TEM column, sodium is highly susceptible to beam-induced reactions. As shown in Figure S7, initial lattice-resolved imaging of Na metal is possible at room temperature at a cumulative dose of ~200 e/Å^2, with the Na (110) planes clearly identified via Fourier analysis. However, further electron exposure rapidly alters the chemical nature of the sample. At a total dose of ~390 e/Å^2, the crystalline Na signal disappears, and ring-like features corresponding to Na_2CO_3 emerge, indicating beam-accelerated oxidation and carbonation processes. Therefore, cryogenic imaging conditions are imperative for preserving native Na morphology and chemistry during high-resolution TEM analysis (Figure S8).

Protocols for mitigating the reactivity of SEI to electron beam

In previous studies, cryo-TEM has identified several inorganic components in the SEI of electrochemically deposited alkali metals.[8,26–29] Although these studies have recognized the electron-sensitive nature of SEI components, detailed imaging conditions, including electron beam dose limitations, have rarely been reported.[18] In this study, we also quantify the electron irradiation damage process of these SEI components at different temperatures. This is a critical step because it determines what dosage parameters are available for minimizing the damage. The mechanisms of electron irradiation damage can be broadly categorized into atomic displacement damage (electron-nucleus interactions) and radiolysis (electron-electron interactions).[30] Displacement damage occurs when high-energy electrons transfer energy and momentum to the nucleus, potentially displacing atoms if enough energy is transferred. This effect is more common at higher accelerating voltages and can displace atomic nuclei to interstitial positions, degrading crystalline structures and creating disordered

Please cite this article in press as: Bai et al., Guidelines for correlative imaging and analysis of reactive alkali metal battery materials, Joule (2025), https://doi.org/10.1016/j.joule.2025.102311

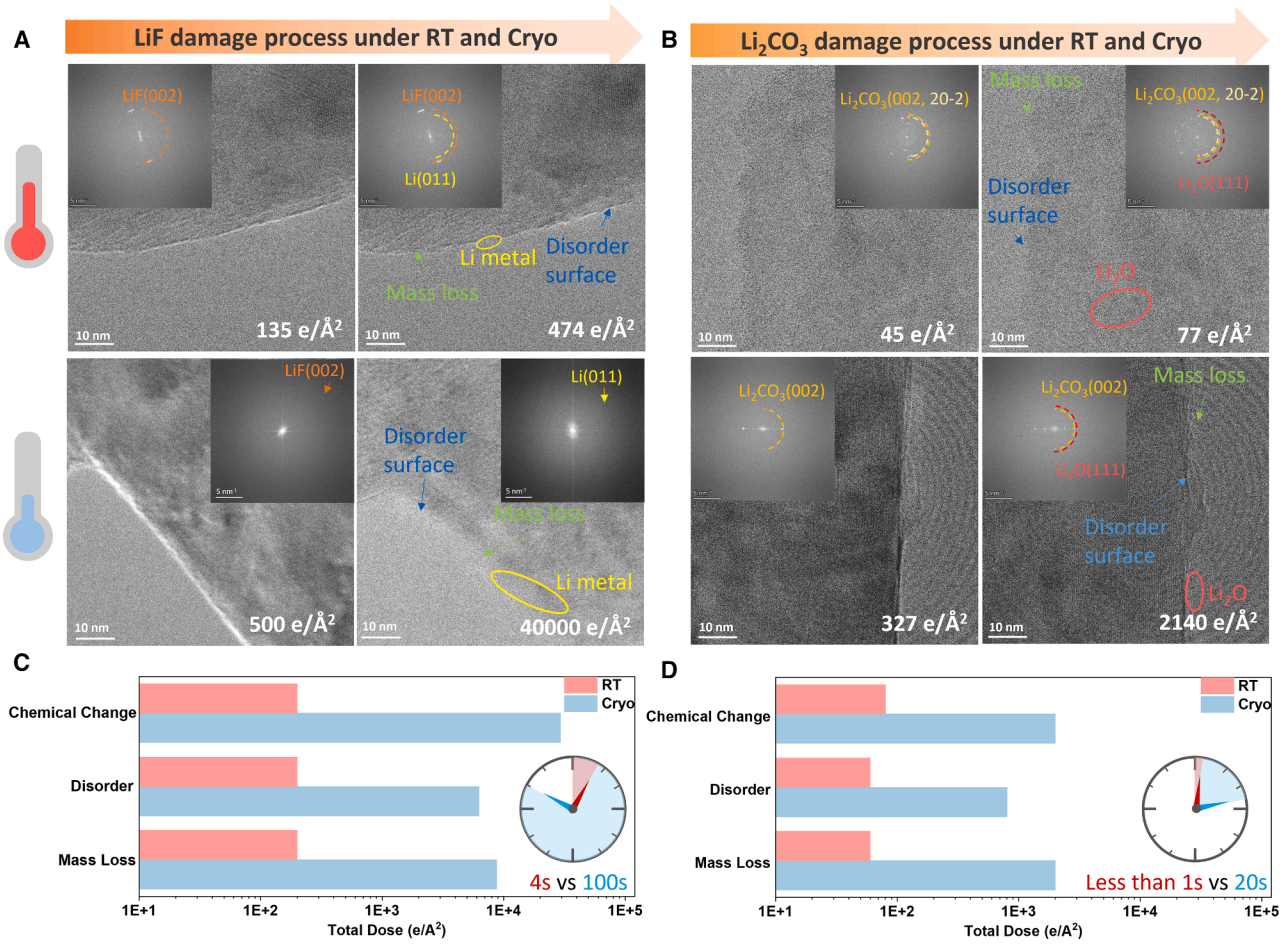

Figure 3. Electron beam-induced damage process and threshold for LiF and Li_2CO_3

(A and B) The damage process to the SEI components LiF (A) and Li_2CO_3 (B) at room temperature (20°C, top panel) and cryo temperature (<−170°C, bottom panel), respectively.

(C and D) Critical total dose threshold of damage process for LiF (C) and Li_2CO_3 (D) at room and cryogenic temperature, respectively. The insets represent the calculated operation time window at a dose rate of 100 e/Å^2·s. The critical beam dose threshold for each SEI compound was defined as the total accumulated dose at which the first irreversible beam-induced change became detectable. Structural disorder was identified by the disappearance of lattice fringes in high-resolution TEM or changes in FFT-derived d-spacings indicating phase transformation (chemical change). Morphological degradation, including particle shrinkage, void formation, or surface rounding, was used to identify the onset of beam-induced mass loss.

regions. As shown in Figure 3, this damage to SEI components is evident in the early stages of imaging, especially at room temperature. Notably, when high-energy scattering occurs in thin specimens or at their surface, the energy required for displacement is significantly reduced, leading to mass loss from subsequent diffusion of reactive intermediates to the surface. Here, we illustrate the time evolution and change of the structure of the SEI components under controlled irradiation experiments. Documented in Figure 3 is the morphological change in high-resolution TEM images with increasing dose at room temperature and when cooled to liquid nitrogen temperatures. The insets in Figures 3A and 3B display fast Fourier transforms (FFTs) taken of the TEM images and allow changes in the spacing of phase contrast lattice images to be tracked as a function of dose.

Additionally, radiolysis occurs due to the interaction between incoming electrons and specimen electrons, which can cause beam heating, bond disruption, and chemical reactions.[31] In the case of LiF, electron beam irradiation reduces the lithium fluoride, resulting in the formation of lithium metal (Figure 3A). This reduction produces metallic lithium nanoparticles within the damaged area. After that, as seen in Figure 3A, these *in situ*-formed Li particles, due to their ultra-small size, readily react with residual oxygen in the TEM column, forming Li_2O. Under cryogenic conditions, LiF still decomposes into lithium metal but with significantly higher dose tolerance. The decreased Li_2O formation is observed as well. The reduction in Li_2O under cryogenic conditions can be attributed to the lower initial amount of *in situ* formed metallic lithium and its reduced oxidation activity at low temperatures. For Li_2CO_3 (Figure 3B), decomposition leads to the formation of Li_2O and the presumed release of CO_2 as a byproduct—a process characteristic of radiolysis that occurs even under low-dose rate conditions (15.9 e/Å^2·s)

Please cite this article in press as: Bai et al., Guidelines for correlative imaging and analysis of reactive alkali metal battery materials, Joule (2025), https://doi.org/10.1016/j.joule.2025.102311

at room temperature. Under cryogenic conditions, a similar damage process is observed, but with >300 times higher beam tolerance (Figure 3B).

The total beam dose limitations for the electron-reactive SEI components related to Li metal anode collected in this study are summarized in Figures 3C, 3D, and S9 for both room temperature (20°C) and cryo temperature (−170°C). The threshold increases significantly from Li_2CO_3, LiF, to Li_2O and lithium metal, which well explains that electron beam damage products in the above-mentioned standard samples are either Li_2O or Li metal. If we take the image at a low-dose mode of 100 e/Å^2·s dose rate, the operation time window for LiF is 4 s at room temperature and 100 s under cryo-condition, while for Li_2CO_3 is less than 1 s and 20 s, respectively. While changing the acceleration voltage does not enhance the dose limit for imaging the SEI component at room temperature (Tables S1 and S2), our observations in Figure 3 highlight the critical role of cryogenic temperatures in mitigating electron damage to SEI components. It should also be noted that electron beam damage is not solely determined by the total accumulated dose but is strongly influenced by the dose rate and irradiation time. Consequently, even at identical cumulative doses, the mechanism and severity of beam-induced damage can differ substantially with exposure conditions.

The differences in total dose thresholds arise primarily from distinct material properties, such as bond strength and atomic weight of the constituent atoms. Bond strength can be estimated by decomposition enthalpy because it reflects the energy required to break a chemical bond. The decomposition enthalpy for LiF is calculated to be 616.0 kJ/mol, which is much higher than that of Li_2CO_3 (226.7 kJ/mol) based on the following reactions:

$$LiF\ (s)\ =\ Li\ (s) + \frac{1}{2}\ F_2\ (g)$$

$$Li_2CO_3\ (s)\ =\ Li_2O\ (s) + CO_2(g)$$

Stronger bonds require more energy to cleave, resulting in higher decomposition enthalpies. Comparing the magnitude of decomposition enthalpies provides insights into why Li_2CO_3 decomposes at a significantly lower total electron dose.

The electron beam damage behavior of sodium SEI components was then evaluated and contrasted with their lithium analogs. As shown in Figure 4, both NaF and Na_2CO_3 experience rapid beam-induced mass loss, surface disordering, and chemical reduction. In NaF, beam doses above ~1,800 e/Å^2 at room temperature induce partial conversion to metallic Na, a phenomenon similar to LiF reduction. However, a key distinction arises in the Na_2CO_3 system: while Li_2CO_3 decomposes first to Li_2O and then to Li metal, Na_2CO_3 bypasses any detectable Na_2O intermediate even at modest doses (~150–900 e/Å^2). The absence of Na_2O intermediate decomposition product is mainly due to the greater beam sensitivity of Na_2O compared with Li_2O, as confirmed in Figure S10. The comparatively lower beam and electrochemical stability of Na_2O relative to Li_2O can be understood from fundamental thermodynamic considerations. The larger ionic radius of Na^+ compared with Li^+ results in a lower lattice energy and weaker Na–O bond strength, leading to reduced cohesive stability of Na_2O. Quantitatively, the beam tolerance of Na_2CO_3 at room temperature is ~20 e/Å^2 before damage initiates, corresponding to an exposure time window of <1 s at a 100 e/Å^2·s dose rate. Under cryogenic conditions, beam tolerance improves by an order of magnitude, extending to ~9 s for Na_2CO_3 and over 100 s for NaF. Note the damaging processes of all the SEI components were recorded using a low-dose technique (<20 e/Å^2·s). This low electron dose rate for atomic-resolution imaging is beyond the capability of conventional complementary metal-oxide semiconductor (CMOS) camera acquisition. Essential to achieve this will be cryogenic resources configured for operation at low dose (<100 e/Å^2·s) using direct electron detectors.

Beyond minimizing imaging artifacts, quantifying beam-induced SEI degradation offers valuable insight into the intrinsic electrochemical stability of SEI components. In alkali metal batteries, SEI breakdown at the anode typically occurs via reduction, making electron-induced radiolysis a relevant proxy for evaluating SEI durability under electrochemical conditions. Our results show that carbonate-based SEIs (e.g., Li_2CO_3 and Na_2CO_3) exhibit the lowest electron dose tolerance, aligning with prior reports identifying them as the least stable SEI species.[32] Conversely, Li_2O—shown to be the most beam-resistant Li SEI phase—is also enriched in high Coulombic efficiency electrolytes (Figure S11).[32] Extending this principle to sodium systems, the comparable beam tolerance of NaF and Na_2O suggests that these species may play a similarly stabilizing role for Na metal anodes. This correlation offers a mechanistic rationale for the higher average Coulombic efficiencies often observed in Na metal electrolytes.[8] While electron beam irradiation and electrochemical degradation occur under fundamentally different conditions, both processes appear sensitive to intrinsic bond stability and chemical composition. Further work combining *operando* electrochemical and low-dose EM could clarify how these correlations may inform SEI design.

Standard protocols for correlative imaging of reactive alkali metal

The results above suggest the critical need for precise control and transparent reporting of cryo-TEM experimental conditions in alkali metal battery research to ensure data reproducibility across studies. Accurately replicating the sample storage environment and documenting key parameters—such as beam energy, total dose, and dose rate—are essential for meaningful interpretation. Since the first cryo-EM reports on lithium metal and SEI materials in 2017, the technique has gained broad adoption across energy systems, including lithium-ion, sodium-ion, lithium-sulfur, solid-state, and polymer-based batteries (Figure 5A). We reviewed 66 key publications (Tables S3 and S4) that apply cryo-EM to lithium metal systems and found that a majority did not report beam dose, a fundamental parameter for evaluating beam-induced damage. Specifically, >80% of solid-state and ~60% of liquid-electrolyte studies omitted this information. As shown in Figure 5B, of the few that did, only 2 (solid) and 11 (liquid) used low-dose imaging, suggesting that less than 20% of studies explicitly control for electron beam effects, raising concerns about the accuracy and comparability of the resulting structural data. Figure 5C summarizes reported SEI components

Please cite this article in press as: Bai et al., Guidelines for correlative imaging and analysis of reactive alkali metal battery materials, Joule (2025), https://doi.org/10.1016/j.joule.2025.102311

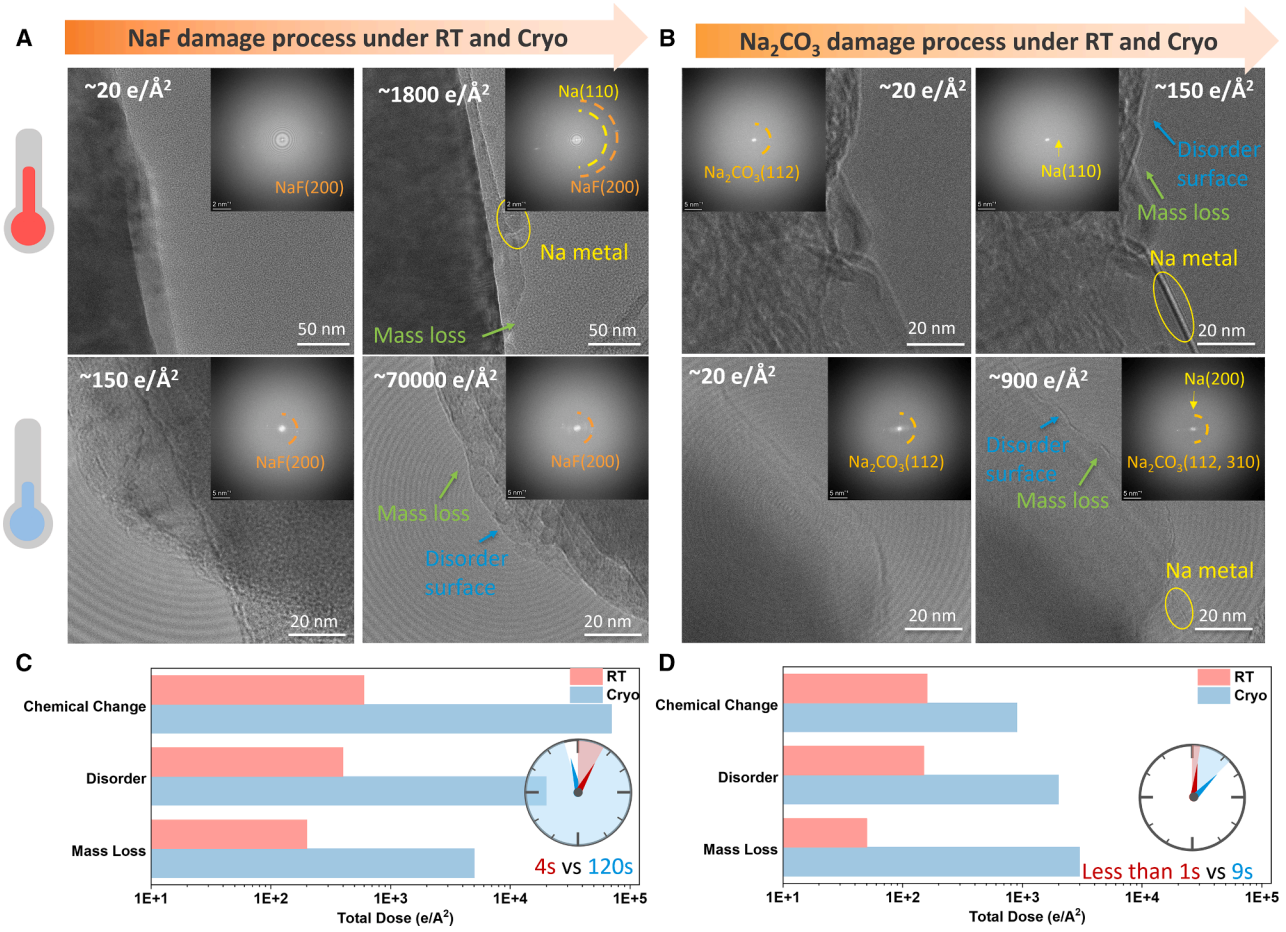

Figure 4. Electron beam-induced damage process and threshold for NaF and Na_2CO_3

(A and B) The damage process to the SEI components NaF (A) and Na_2CO_3 (B) at room temperature (20°C, top panel) and cryo temperature (<−170°C, bottom panel), respectively.

(C and D) Critical total dose threshold of damage process for NaF (C) and Na_2CO_3 (D) at room and cryogenic temperature, respectively. The insets represent the calculated operation time window at a dose rate of 100 e/Å^2·s.

and crystallographic phases in liquid-electrolyte systems for Li metal anodes. Li_2O appears most frequently (>35%), followed by LiF, Li_2CO_3, and less common species such as LiOH and Li_2S. While lattice-resolved imaging confirms the presence of crystalline phases, few studies explore the functional role of Li_2O within the SEI. Its origin remains unclear—either intrinsic to specific chemistry or, as our data suggest, a beam-induced product formed through radiolysis of LiF or Li_2CO_3.

The literature summary reveals a lack of standardized protocols for handling beam-sensitive battery materials like lithium metal during TEM studies. The assumption that cryogenic imaging alone preserves sample integrity is overly simplistic. Meaningful cross-sample comparison must include explicit control or reporting of parameters such as specimen thickness, particle size, synthesis/preparation history, accelerating voltage, dose rate and cumulative dose, imaging mode, temperature, vacuum/transfer conditions, and pre-exposure history. These variables critically influence electron-matter interactions and beam tolerance. In practical battery systems, SEI components are typically non-uniform in thickness and composition, making it more relevant to evaluate beam damage in samples that reflect this complexity. Therefore, while we acknowledge that the precise numerical thresholds may not be universally applicable, the methodology we employed is well-suited for establishing practical dose guidelines in real-world cryo-TEM investigations of SEI materials. Encouragingly, for studies focused on bulk lithium metal rather than SEI interfaces, room-temperature TEM imaging at atomic resolution is feasible with optimized preparation and minimal air exposure.

In addition to the urging of reporting detailed experimental conditions for cryo-EM, equally critical is the establishment of reliable criteria to identify the onset of electron beam damage during imaging of reactive or beam-sensitive samples. Structural degradation can manifest in reciprocal space as fading or broadening of diffraction spots, loss of lattice fringes in high-resolution TEM, or changes in FFT patterns indicating amorphization. In real space, damage indicators include morphological evolution such as particle shrinking, void formation, rounding of edges,

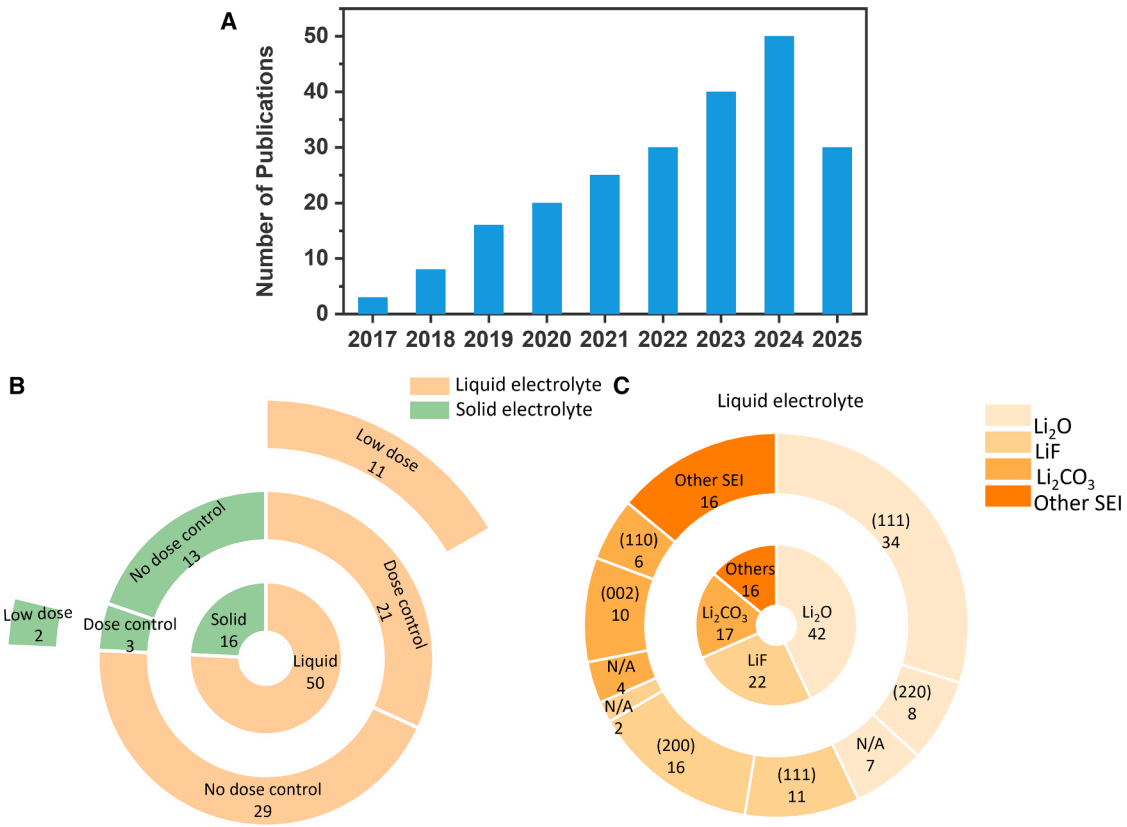

Figure 5. Literature summary of research associated with the (S)TEM study on the SEI in battery materials

(A) Numbers of publications each year since the introduction of cryo-EM into the battery research field.

(B) Numbers under each label represent the number of publications on cryo-EM analysis for lithium metal battery study.

(C) Numbers of SEI components and crystallographic lattices identified in lithium metal batteries with conventional organic solvent-based electrolytes. Here, we classify low dose to indicate TEM imaging acquisition at the electron dose rate less than 100 e/Å^2·s.

or the buildup of bubble-like features on the surface. Misidentification is common when these effects are not distinguished from intrinsic structural heterogeneity.[33] Processing the resulting high-resolution images from SEI studies can also present significant challenges due to the nature of the complexity of materials in the system and the large amount of data produced. The complex materials characterization technologies embodied in the cryogenic imaging and analysis protocols are an inefficient method for comprehensive characterization of energy materials when driven by a human. Site-to-site variation and the sample preparation procedures further increase the difficulty of claiming a fully comprehensive representation of material systems.

To tackle this problem, a novel workflow is applied for detecting components and phase segmentation from raw high-resolution TEM images using a deep learning-trained model.[34] As shown in Figures S12 and S13, the developed model can expedite the phase segmentation along the electron beam irradiation damage process for both LiF and Li_2CO_3, diminishing the temporal and cognitive demands associated with scrutinizing an extensive array of TEM images, thereby allowing us to apply both low-dose and time-intensive analytical electron microscopy techniques. The model, trained primarily on alkali metal and SEIs, provides reliable phase identification under similar contrast and imaging conditions. Its direct transfer to other chemistries (e.g., sulfide interphases) would require additional fine-tuning with representative datasets. Limitations include potential sensitivity to beam-induced morphology changes and microscope-specific contrast variations. Despite these constraints, this workflow substantially reduces manual analysis time and establishes a foundation for community-wide adoption of standardized, automated segmentation tools in energy-materials imaging.

Building on our understanding of alkali metal's chemical reactivity, we present a protocol for high-resolution characterization, minimizing changes from beam sources or environmental factors. This process integrates storage, preparation, transfer, and characterization for correlative imaging down to the atomic scale. Taking Li metal as an example, as shown in Figure 6, the protocol starts with loading the bulk lithium metal onto the IGST system in the glovebox, where it is stored for up to 2 days before transfer to the PFIB-SEM. Lamella preparation, including milling, lift out, and thinning, is done at cryogenic temperatures to prevent contamination. Multiple lamellas with two windows each are prepared for high-resolution TEM, taking under an hour, compared with 5–10 h with

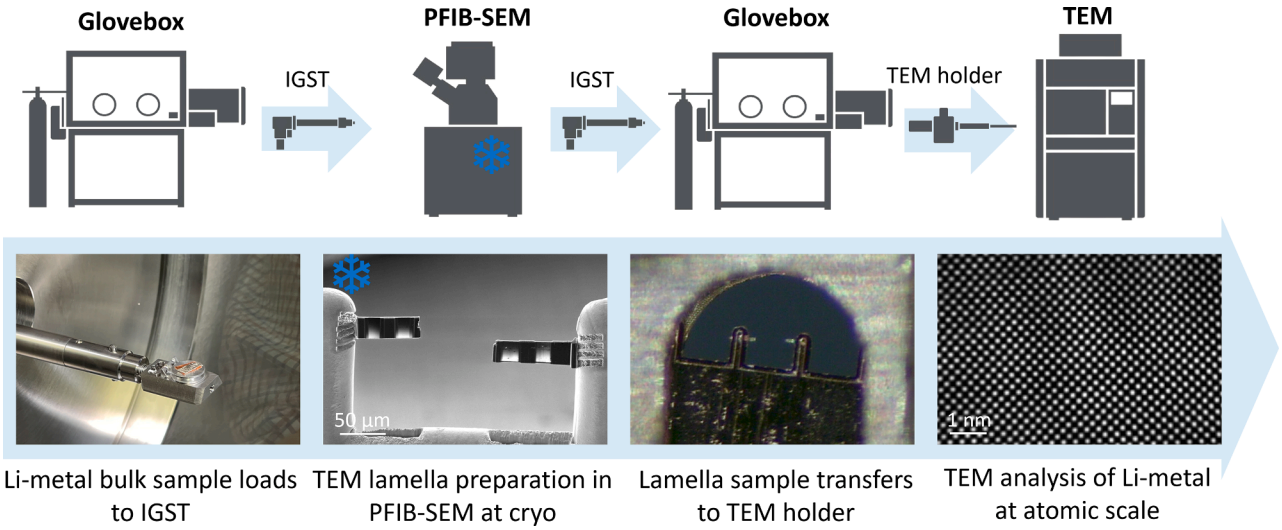

Figure 6. Correlative imaging workflow for PFIB-TEM characterization through IGST to preserve reactive lithium metal in its native state
The snowflake icon indicates the characterization at cryogenic temperature.

Ga^+ FIB. After PFIB, lamellas are transferred back to the glovebox under Ar protection and then to the TEM via an inert gas transfer holder. The success of this protocol relies on continuous inert gas protection, inert ion preparation, minimal glovebox storage, and the inert gas transfer holder (Table S5), laying the foundation for room-temperature imaging of Li metal at atomic resolution.

Conclusions

This work presents a comprehensive framework for the preparation, storage, transfer, and correlative imaging of reactive alkali metal electrodes, with a focus on lithium and sodium systems. We demonstrate that using inert ion sources such as Xe^+ or Ar^+ in PFIB enables damage-free lamella preparation, while minimizing glovebox storage time and employing IGST is essential to preserve sample integrity. High-resolution TEM imaging of lithium metal is achievable at room temperature; however, SEI components like Li_2CO_3 and LiF are highly beam-sensitive, requiring low-dose cryogenic imaging to avoid misinterpretation from beam-induced reduction to Li_2O or lithium metal. Extending this analysis to sodium, we find Na metal is even more environmentally reactive than Li, demanding more rigorous cryogenic handling. Sodium metal-related SEIs also exhibit distinct beam sensitivity—most notably, Na_2O is far less stable than Li_2O—highlighting the need for metal-specific SEI design rather than direct translation from Li systems. These findings provide a mechanistic link between electron-beam sensitivity and electrochemical stability, offering a new perspective on interfacial engineering for high-efficiency alkali metal batteries. Finally, our study emphasizes the need for standardized cryo-EM protocols and dose reporting. Future directions include deep learning-assisted image analysis and correlative multimodal characterization (e.g., X-ray, neutron depth profiling, nuclear magnetic resonance) to further advance high-fidelity, artifact-free imaging of reactive battery materials.

METHODS

Materials

Li_2CO_3 (99.99%), LiF (>99.98%), and Li_2O (>99.98%) were obtained from Sigma-Aldrich. NaF (>99%), Na_2CO_3 (99.5%), and Na_2O (>99%) were purchased from Fisher Scientific. These powders were carefully ground by hand using a mortar and pestle for 5 min in an Ar-filled glovebox. Li metal foil was purchased from MTI Corporation. Battery-grade lithium bis(fluorosulfonyl)imide (LiFSI) was purchased from Oakwood Products, Inc., and bis(trifluoromethane)sulfonimide lithium 99.95% (LiTFSI) was purchased from Sigma-Aldrich. All salts were further dried at 120°C under vacuum for 24 h before use, and DME anhydrous, 99.5%, was purchased from Sigma-Aldrich. Solvents were dried with molecular sieves before use. LiFSI-LiTFSI was mixed in a molar ratio of 4.7:2.3 in DME to prepare the bisalt electrolyte. Gen2 electrolyte was purchased from Gotion, Inc.

Electrochemical measurements

A custom-made split cell with two titanium plungers and one polyether ether ketone (PEEK) die mold (all 1/2-inch inner diameter) was used for the Li deposition in the Li storage test. The Cu||Li cells were made by layering the Li metal foil (7 mm diameter, 50 μm thick, China Energy Lithium Co., Ltd.), Celgard 2325 separator (1/2 inch diameter), and the cleaned Cu foil between the two titanium plungers inside the PEEK die mold. Only ~5 μL of electrolyte was added to the Cu||Li cells to wet the separator. After the assembly, the split cell and the load cell were put into the cell holder, which provided the uniaxial stacking pressure at 350 kPa. The cell was tested inside the glovebox using Landt CT2001A battery cycler (Wuhan, China). Li metal was deposited to 0.25 mAh/cm^2 with a current density of 2 mA/cm^2 in both electrolytes.

TGC

The TGC method was used to quantify the amount of inactive metallic Li formed after various storage times. After the storage,

Please cite this article in press as: Bai et al., Guidelines for correlative imaging and analysis of reactive alkali metal battery materials, Joule (2025), https://doi.org/10.1016/j.joule.2025.102311

the commercial Li or deposited Li with Cu was collected and put into a 30 mL bottle without washing. The bottle was sealed with a rubber stopper to prevent gas leakage and potential safety hazards. The internal pressure of the container was then adjusted to the equilibrium of the glovebox environment, whose internal pressure has been adjusted to 1 atm, with an open-ended syringe needle. After taking out the bottle from the glovebox, an excessive amount (0.5 mL) of deionized (DI) water was introduced into the bottle, and H_2 gas was generated due to the reaction between water and reactive metallic Li in the system. The as-generated gas was then well mixed by shaking, and 30 μL mixed gas was then injected into the Nexis GC2030 Gas Chromatograph (Shimadzu) for H_2 measurement. A pre-established H_2 calibration curve was used to calculate the mass of metallic Li by measuring the H_2 peak area. At least three samples were tested for each measurement point by TGC.

PFIB-SEM

The PFIB-SEM work was conducted on a Thermo Scientific Helios 5 Hydra UX DualBeam. For the chemical reactivity analysis study using Xe^+ ions, the cross-section of the commercial Li metal (MTI Corp.) was prepared using 30 kV ions, starting from 1 μA for the bulk cross-section, followed by 200 nA and 60 nA for the cleaning cross-section. A tungsten protective cap was prepared before cross-section milling, and a rocking mill was applied to improve the cross-section cutting quality. The SEM imaging was collected via through-the-lens detector secondary electron (TLD-SE) detector at 2 keV and 0.4 nA. EDS was collected at 5 keV via the Oxford Ultim Max EDS detector.

For the chemical reactivity analysis using Ar^+ ions, the cross-section of the commercial Li metal (MTI Corp.) was prepared using 30 kV, starting from 4 μA for the bulk cross-section, followed by 2 μA and 120 nA for the cleaning cross-section. The SEM imaging was collected via TLD-SE detector at 2 keV and 0.4 nA.

For the cross-section of commercial Li metal prepared at a cryogenic temperature of −170°C, a tungsten capping layer was deposited on the sample surface before cross-section using 30 kV Xe^+ ions, starting from 1 μA for bulk cross-section, followed by 200 nA and 60 nA for cleaning cross-section.

Standard protocols for correlative imaging of reactive Li metal

Sample loading in glovebox and transfer. Li foil stored in a glovebox was first glued onto an aluminum stub with double-sided copper tape. To ensure Li freshness, the top surface of the glued Li foil was scraped with a razor blade inside the glovebox. The mounted Li foil sample was then loaded onto a Thermo Scientific CleanConnect sample transfer system together with a small TEM grid holder, which holds a 3 mm TEM grid for FIB lamella. The IGST system then transferred the sample out of the glovebox to FIB-SEM for TEM lamella preparation.

Lamella preparation in FIB-SEM. The Li metal TEM lamella was prepared via a Thermo Scientific Helios 5 Hydra FIB-SEM. First, the CleanConnect system system was used to transfer the bulk Li foil and the TEM grid into the FIB-SEM's vacuum sample chamber without exposure to the atmosphere. To stabilize Li metal during milling, the whole shuttle was cooled down with a Thermo Fisher Scientific cryo-stage inside the FIB-SEM to a temperature of <−170°C. Ar^+ ion species were used during the entire TEM lamella-making process.

A FIB current of 120 nA with an acceleration voltage of 30 kV was used to carry out rough milling. The initial Li metal chunk was made, followed by cleaning with 40 nA FIB current under 30 kV and then lifting out from the bulk with a Thermo Scientific cryo Easylift nanomanipulator. The lift-out needle was cooled to <−170°C during the lift-out process to minimize any heat transfer.

The lifted-out Li metal chunk was then mounted to a copper TEM grid under cryo conditions for final thinning. The Li metal chunk was first thinned with a FIB current of 16 nA at 30 kV to about 700 nm in thickness. Then the FIB current was progressively reduced to 0.5 nA until the lamella reached about 300 nm in thickness. Final polishing was then carried out with a FIB acceleration voltage of 5 kV and a beam current of 200 pA. The thinned area of the lamella was then polished to electron transparency with a thickness around 150 nm and was then ready for TEM observation.

Multiple Li metal lamellas were made using the above method. Once lamellas were thinned to electron transparency, the cryo-stage was then warmed up progressively to room temperature. Over 40 min, the stage was warmed up from −178°C to 20°C. The prepared lamellas, together with the bulk Li sample, were then transferred from FIB-SEM's vacuum chamber to the CleanConnect system. The capsule was filled with Ar gas to protect the samples during transfer back to the glovebox.

Lamella transfer to glovebox and sample loading. Once the transfer shuttle arrived at the glovebox, the TEM grids with prepared Li metal lamellas were then transferred to a Mel-Build Atmos Defend TEM holder with a vacuum tweezer. The grid was securely mounted on the holder, and the holder was then manually closed to seal the Ar environment inside the small chamber in the holder to protect the lamellas during the final transfer to TEM. The sealed holder was then transferred out of the glovebox and then loaded into a Thermo Scientific Talos F200X S/TEM for further analysis and imaging.

For the cryo-transfer workflow, the lamella sample was placed in a cryogenic grid box with a sample handling rod, then sealed in a metallized polyester bag. The bag was removed from the glovebox and immediately plunged into liquid nitrogen in a Styrofoam reservoir. The bag was cut open under liquid nitrogen, and the cryogenic grid box was removed and placed in a Gatan Elsa holder stand. The sample was then loaded into the Gatan Elsa cryo-holder under cryogenic conditions and transferred to the TEM under cryogenic conditions. The entire transfer from glovebox to TEM took ~25 min. A 7 min airlock time was used. The sample was imaged at cryogenic temperature.

TEM characterizations. The Thermo Scientific Talos F200X S/TEM, outfitted with a Gatan continuum EELS and a Mel-Build Atmos Defend TEM holder, serves as the primary instrument for Li metal lamellae characterization. Operated at 200 kV under low electron dose conditions, the instrument facilitates the acquisition of high-resolution images with minimal beam-induced specimen damage. The atomic-resolution TEM image was collected at room temperature using a Ceta 16M camera. The dose rate was about 3.5×10^3 e/Å^2 s. With an exposure time of 500 ms, it gives a total dose of 1,750 e/Å.[2]

TEM/STEM studies

The electron beam irradiation damage process of LiF and Li_2CO_3 was measured using the Analytical PicoProbe Electron Optical Beam Line at Argonne National Laboratory (ANL), which is the prototype of the Thermo Scientific Iliad Ultra (S)TEM system. This sub-Angstrom resolution instrument was operated at 60, 200, and 300 kV at both room temperature and cryogenic conditions, as indicated in the main text for various aspects of this work. High-resolution TEM phase contrast images were collected on the Thermo Scientific Falcon 4i Direct Electron Detector under low-dose conditions at $1K^2$ to $4K^2$ pixel resolution with an exposure time ranging from 0.5 to 5 s per frame in streaming acquisition (i.e., movie mode) and operating in both standard as well as the Fresnel Free Imaging Mode. Electron diffraction measurements were conducted using a $1K^2$-$4K^2$ CetaII CMOS camera. Supporting X-ray and electron energy loss spectroscopy were conducted using the 4.5 sR collection angle XPAD and ultrahigh energy resolution Illiad electron spectrometer installed on the instrument. Dose and dose rate measurements were performed using a Faraday cup calibrated beam current monitor together with accurate *in situ* beam size measurements.

Electron damage and spectroscopy studies of Li, Na, and SEI-related materials were studied using an inert gas transfer cryogenic holder from Simple Origin (Model 206) as well as a custom Be-tipped cryo-transfer holder by Fishione Instruments (Model 2550). SEI material samples were prepared by crushing and dry drop casting and, as appropriate, using an argon glovebox system, from which they were *in situ* sealed in the Simple Origin holder and transferred to the TEM at room temperature. Once inserted into the electron microscope, experiments were either conducted at room temperature or cooled to $-170^{\circ}C$ for cryogenic measurements.

RESOURCE AVAILABILITY

Lead contact

Requests for further information and resources should be directed to and will be fulfilled by the lead contact, Ying Shirley Meng (shirleymeng@uchicago.edu).

Materials availability

This study did not generate new, unique reagents.

Data and code availability

Requests for the data and analysis utilized in this work will be handled by the lead contact, Ying Shirley Meng (shirleymeng@uchicago.edu).

ACKNOWLEDGMENTS

The authors acknowledge funding support from the Energy Storage Research Alliance, an Energy Innovation Hub funded by the U.S. Department of Energy, Office of Science, Basic Energy Sciences under DE-AC02-06CH11357. Y.S.M. and N.J.Z. are grateful for the LDRD funding from Argonne National Laboratory. The prototype Thermo Scientific Iliad Ultra (S)TEM system was developed and supported as part of CRADA #01300710 and CRADA #A24560 between Argonne National Laboratory, the University of Chicago, and Thermo Fisher Scientific and was supported in part by the DOE Office of Science by Argonne National Laboratory under contract no. DE-AC02-06CH11357, as well as in part by the National Science Foundation Major Research Instrumentation (MRI) Program (NSF DMR-2117896) at the University of Chicago. The work performed at UC San Diego was also supported by the funding and collaboration agreement between UC San Diego and Thermo Fisher Scientific on Advanced Characterization of Energy Materials. Part of the TEM images are collected at the San Diego Nanotechnology Infrastructure (SDNI), a member of the National Nanotechnology Coordinated Infrastructure, which is supported by the National Science Foundation (grant ECCS-1542148). The authors gratefully acknowledge technical support from Mel-Build and Simple Origin. The authors also thank Thermo Fisher Scientific Americas NanoPort for PFIB-SEM and TEM tests for workflow validation and Ruijie Shao for preparing the Li-metal lamella sample for cryo-transfer holder testing. The authors also acknowledge the assistance from Bing Han for Li_2O data acquisition. T.S.M. acknowledges the support by the National Science Foundation Graduate Research Fellowship under grant no. 214000.

AUTHOR CONTRIBUTIONS

M.Z., Z.L., S.B., and Y.S.M. conceived the ideas and designed the experiments. A.S. conducted PFIB and EDS testing at both room temperature and cryogenic temperature for Li metal. B.L., D.C., and S.B. prepared samples for TGC analysis and analyzed the data. L.L., L.J., B.V.L., J.P.C., R.O., P.B., and A.B. acquired and analyzed the TEM data for Li metal. S.B. and M.C. acquired and analyzed the TEM data for Na metal. N.J.Z., S.B., G.R., and T.S.M. acquired and analyzed the TEM data for SEI components. M.Z. and Y.S.M. supervised the research. S.B., Z.L., S.W., and M.Z. wrote the manuscript. All authors contributed to the discussion and provided feedback on the manuscript.

DECLARATION OF INTERESTS

The authors declare no competing interests.

SUPPLEMENTAL INFORMATION

Supplemental information can be found online at https://doi.org/10.1016/j.joule.2025.102311.

Received: July 14, 2025
Revised: November 14, 2025
Accepted: December 29, 2025

REFERENCES

1. Fang, C., Li, J., Zhang, M., Zhang, Y., Yang, F., Lee, J.Z., Lee, M.H., Alvarado, J., Schroeder, M.A., Yang, Y., et al. (2019). Quantifying inactive lithium in lithium metal batteries. Nature *572*, 511–515. https://doi.org/10.1038/s41586-019-1481-z.
2. Fang, C., Lu, B., Pawar, G., Zhang, M., Cheng, D., Chen, S., Ceja, M., Doux, J.M., Musrock, H., Cai, M., et al. (2021). Pressure-tailored lithium deposition and dissolution in lithium metal batteries. Nat. Energy *6*, 987–994. https://doi.org/10.1038/s41560-021-00917-3.
3. Sayahpour, B., Hirsh, H., Parab, S., Nguyen, L.H.B., Zhang, M., and Meng, Y.S. (2022). Perspective: Design of cathode materials for sustainable sodium-ion batteries. MRS Energy Sustain. *9*, 183–197. https://doi.org/10.1557/s43581-022-00029-9.
4. Deysher, G., Oh, J.A.S., Chen, Y.T., Sayahpour, B., Ham, S.Y., Cheng, D., Ridley, P., Cronk, A., Lin, S.W.H., Qian, K., et al. (2024). Design principles for enabling an anode-free sodium all-solid-state battery. Nat. Energy *9*, 1161–1172. https://doi.org/10.1038/s41560-024-01569-9.
5. Xu, W., Wang, J., Ding, F., Chen, X., Nasybulin, E., Zhang, Y., and Zhang, J.G. (2014). Lithium metal anodes for rechargeable batteries. Energy Environ. Sci. *7*, 513–537. https://doi.org/10.1039/C3EE40795K.
6. Chen, S., Zheng, J., Mei, D., Han, K.S., Engelhard, M.H., Zhao, W., Xu, W., Liu, J., and Zhang, J.G. (2018). High-Voltage Lithium-Metal Batteries Enabled by Localized High-Concentration Electrolytes. Adv. Mater. *30*, e1706102. https://doi.org/10.1002/adma.201706102.

7. Yang, Y., Davies, D.M., Yin, Y., Borodin, O., Lee, J.Z., Fang, C., Olguin, M., Zhang, Y., Sablina, E.S., Wang, X., et al. (2019). High-Efficiency Lithium-Metal Anode Enabled by Liquefied Gas Electrolytes. Joule *3*, 1986–2000. https://doi.org/10.1016/j.joule.2019.06.008.

8. Sayahpour, B., Li, W., Bai, S., Lu, B., Han, B., Chen, Y.T., Deysher, G., Parab, S., Ridley, P., Raghavendran, G., et al. (2024). Quantitative analysis of sodium metal deposition and interphase in Na metal batteries. Energy Environ. Sci. *17*, 1216–1228. https://doi.org/10.1039/D3EE03141A.

9. Sood, A., Poletayev, A.D., Cogswell, D.A., Csernica, P.M., Mefford, J.T., Fraggedakis, D., Toney, M.F., Lindenberg, A.M., Bazant, M.Z., and Chueh, W.C. (2021). Electrochemical ion insertion from the atomic to the device scale. Nat. Rev. Mater. *6*, 847–867. https://doi.org/10.1038/s41578-021-00314-y.

10. Xu, K. (2014). Electrolytes and interphases in Li-ion batteries and beyond. Chem. Rev. *114*, 11503–11618. https://doi.org/10.1021/cr500003w.

11. Zhang, M., Chouchane, M., Shojaee, S.A., Winiarski, B., Liu, Z., Li, L., Pelapur, R., Shodiev, A., Yao, W., Doux, J.M., et al. (2023). Coupling of multi-scale imaging analysis and computational modeling for understanding thick cathode degradation mechanisms. Joule *7*, 201–220. https://doi.org/10.1016/j.joule.2022.12.001.

12. Cheng, D., Lu, B., Raghavendran, G., Zhang, M., and Meng, Y.S. (2022). Leveraging cryogenic electron microscopy for advancing battery design. Matter *5*, 26–42. https://doi.org/10.1016/j.matt.2021.11.019.

13. Han, B., Li, X., Bai, S., Zou, Y., Lu, B., Zhang, M., Ma, X., Chang, Z., Meng, Y.S., and Gu, M. (2021). Conformal three-dimensional interphase of Li metal anode revealed by low-dose cryoelectron microscopy. Matter *4*, 3741–3752. https://doi.org/10.1016/j.matt.2021.09.019.

14. Li, Y., Li, Y., Pei, A., Yan, K., Sun, Y., Wu, C.L., Joubert, L.M., Chin, R., Koh, A.L., Yu, Y., et al. (2017). Atomic structure of sensitive battery materials and interfaces revealed by cryo–electron microscopy. Science *358*, 506–510. https://doi.org/10.1126/science.aam6014.

15. Wang, X., Zhang, M., Alvarado, J., Wang, S., Sina, M., Lu, B., Bouwer, J., Xu, W., Xiao, J., Zhang, J.G., et al. (2017). New Insights on the Structure of Electrochemically Deposited Lithium Metal and Its Solid Electrolyte Interphases via Cryogenic TEM. Nano Lett. *17*, 7606–7612. https://doi.org/10.1021/acs.nanolett.7b03606.

16. Wang, X., Pawar, G., Li, Y., Ren, X., Zhang, M., Lu, B., Banerjee, A., Liu, P., Dufek, E.J., Zhang, J.G., et al. (2020). Glassy Li metal anode for high-performance rechargeable Li batteries. Nat. Mater. *19*, 1339–1345. https://doi.org/10.1038/s41563-020-0729-1.

17. Lee, J.Z., Wynn, T.A., Schroeder, M.A., Alvarado, J., Wang, X., Xu, K., and Meng, Y.S. (2019). Cryogenic Focused Ion Beam Characterization of Lithium Metal Anodes. ACS Energy Lett. *4*, 489–493. https://doi.org/10.1021/acsenergylett.8b02381.

18. Zachman, M.J., Tu, Z., Choudhury, S., Archer, L.A., and Kourkoutis, L.F. (2018). Cryo-STEM mapping of solid–liquid interfaces and dendrites in lithium-metal batteries. Nature *560*, 345–349. https://doi.org/10.1038/s41586-018-0397-3.

19. Liang, C., Zhang, X., Xia, S., Wang, Z., Wu, J., Yuan, B., Luo, X., Liu, W., Liu, W., and Yu, Y. (2020). Unravelling the room-temperature atomic structure and growth kinetics of lithium metal. Nat. Commun. *11*, 5367. https://doi.org/10.1038/s41467-020-19206-w.

20. Liu, Z., Bai, S., Burke, S., Burrow, J.N., Geurts, R., Huang, C.J., Jiao, C., Lee, H.B., Meng, Y.S., Novák, L., et al. (2025). FIB-SEM: Emerging Multimodal/Multiscale Characterization Techniques for Advanced Battery Development. Chem. Rev. *125*, 5228–5281. https://doi.org/10.1021/acs.chemrev.4c00831.

21. Xiao, J. (2019). How lithium dendrites form in liquid batteries. Science *366*, 426–427. https://doi.org/10.1126/science.aay8672.

22. Wang, X., Li, Y., and Meng, Y.S. (2018). Cryogenic Electron Microscopy for Characterizing and Diagnosing Batteries. Joule *2*, 2225–2234. https://doi.org/10.1016/j.joule.2018.10.005.

23. Krishnaswamy, S.R., Gabrovski, I.A., Patmanidis, I., Stuart, M.C.A., de Vries, A.H., and Pshenichnikov, M.S. (2022). Cryogenic TEM imaging of artificial light harvesting complexes outside equilibrium. Sci. Rep. *12*, 5552. https://doi.org/10.1038/s41598-022-09496-z.

24. Rigort, A., Villa, E., Bäuerlein, F.J.B., Engel, B.D., and Plitzko, J.M. (2012). Integrative Approaches for Cellular Cryo-electron Tomography: Correlative Imaging and Focused Ion Beam Micromachining. Methods Cell Biol. *111*, 259–281. https://doi.org/10.1016/B978-0-12-416026-2.00014-5.

25. Zhai, W., Yuan, B., Fan, Y., Zhang, Y., Zhang, X., Ma, Y., Liu, W., and Yu, Y. (2022). Microstructure of Lithium Dendrites Revealed by Room-Temperature Electron Microscopy. J. Am. Chem. Soc. *144*, 4124–4132. https://doi.org/10.1021/jacs.1c13213.

26. Li, Y., Huang, W., Li, Y., Pei, A., Boyle, D.T., and Cui, Y. (2018). Correlating Structure and Function of Battery Interphases at Atomic Resolution Using Cryoelectron Microscopy. Joule *2*, 2167–2177. https://doi.org/10.1016/j.joule.2018.08.004.

27. Liu, Y., Tao, X., Wang, Y., Jiang, C., Ma, C., Sheng, O., Lu, G., and Lou, X.W.D. (2022). Self-assembled monolayers direct a LiF-rich interphase toward long-life lithium metal batteries. Science *375*, 739–745. https://doi.org/10.1126/science.abn1818.

28. Cao, X., Ren, X., Zou, L., Engelhard, M.H., Huang, W., Wang, H., Matthews, B.E., Lee, H., Niu, C., Arey, B.W., et al. (2019). Monolithic solid–electrolyte interphases formed in fluorinated orthoformate-based electrolytes minimize Li depletion and pulverization. Nat. Energy *4*, 796–805. https://doi.org/10.1038/s41560-019-0464-5.

29. Huang, W., Wang, H., Boyle, D.T., Li, Y., and Cui, Y. (2020). Resolving Nanoscopic and Mesoscopic Heterogeneity of Fluorinated Species in Battery Solid-Electrolyte Interphases by Cryogenic Electron Microscopy. ACS Energy Lett. *5*, 1128–1135. https://doi.org/10.1021/acsenergylett.0c00194.

30. Egerton, R.F., Li, P., and Malac, M. (2004). Radiation damage in the TEM and SEM. Micron *35*, 399–409. https://doi.org/10.1016/j.micron.2004.02.003.

31. Jiang, N. (2015). Electron beam damage in oxides: a review. Rep. Prog. Phys. *79*, 016501. https://doi.org/10.1088/0034-4885/79/1/016501.

32. Hobold, G.M., Wang, C., Steinberg, K., Li, Y., and Gallant, B.M. (2024). High lithium oxide prevalence in the lithium solid–electrolyte interphase for high Coulombic efficiency. Nat. Energy *9*, 580–591. https://doi.org/10.1038/s41560-024-01494-x.

33. Deng, Y.H., and Nest, L.G. (2021). Analysis of misidentifications in TEM characterisation of organic-inorganic hybrid perovskite material. J. Microsc. *282*, 195–204. https://doi.org/10.1111/jmi.13000.

34. Raghavendran, G., Han, B., Adekogbe, F., Bai, S., Lu, B., Wu, W., Zhang, M., and Meng, Y.S. (2025). Deep learning assisted high-resolution microscopy image processing for phase segmentation in functional composite materials. J. Microsc., 1–16. https://doi.org/10.1111/jmi.13413.